ORIGINAL ARTICLE

lajss.org©
Latin American Journal of Solids and Structures

www.lajss.org

Penetration of ballistic gelatin by explosion-driven inert metal particles

Weihang Li[a], Wenjin Yao[a*], Wei Zhu[a], Wenbin Li[a], Dacheng Gao[a], Shilei Tian[b], Chao Han[b], Yangyang Liu[b]

[a]Ministerial Key Laboratory of ZNDY, Nanjing University of Science and Technology, Nanjing, Jiangsu, China. Email: lwh2020@njust.edu.cn, njyaowj@163.com, 12021059@njust.edu.cn, lwb2000cn@njust.edu.cn, gaodacheng001@163.com

[b]Hebei Second Machinery Industry Co., Ltd, Shijiazhuang, Hebei, China. Email: tianshileihg@163.com, 393574476@qq.com, 305903034@qq.com

* Corresponding author

https://doi.org/10.1590/1679-78258015

Abstract

In urban combat, sub-millimeter inert metal powder is used to replace fragments in explosive bombs, which can effectively reduce collateral damage. In order to investigate the damage effect of high-speed metal particles on the human body, a particle ring filled with a charge was designed to create an explosion-driven particle cloud for the penetration ballistic gelatin. The particle ring was made of polytetrafluoroethylene (PTFE) and sub-millimeter tungsten powder. The dispersion properties of the particle cloud driven by the explosion were studied with high-speed photography and ballistic gelatin. Furthermore, the numerical simulation models of particle-penetrating gelatin based on the experimental results were established with the finite element method. The influences of the particle size and velocity on the penetration depth and cavity diameter was obtained. The relationship between the critical interference distance of the cavity and the distance between particles was determined. This paper provides references and theoretical support for the design of low collateral damage ammunition based on inert metal powder.

Keywords

low collateral damage; tungsten powder; PTFE; ballistic gelatin; temporary cavity

Graphical Abstract

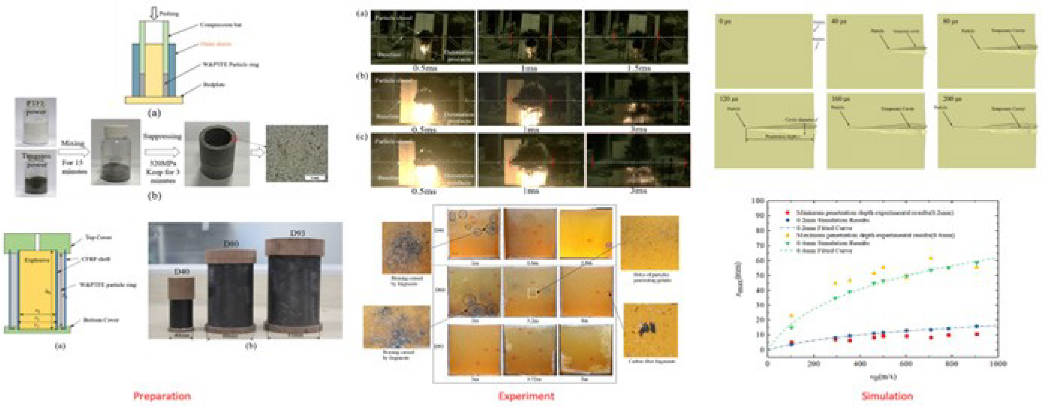

Received: January 30, 2024. In revised form: January 31, 2024. Accepted: February 12, 2024. Available online: February 20, 2024
https://doi.org/10.1590/1679-78258015

1 INTRODUCTION

In recent decades, local armed conflicts and terrorism have become more frequent. Statistics from the Global Terrorism Database (GTD) show there were over 100,000 terrorist attacks between 2005 and 2019. Most terrorist attacks occur in densely populated urban environments and civilians are often close to the terrorists during an engagement. Therefore, avoiding civilian casualties when eliminating terrorists must be considered in anti-terrorism operations (Walsh. 2014). Fragmentation bombs that can produce high-speed metal fragments are very effective in eliminating enemy personnel who are within the killing radius. However, those bombs are not suitable for anti-terrorism operations because the fragments still have a large range of lethality when flying outside of the killing radius, which is the so-called high collateral lethality. Therefore, extensive research has been conducted to develop low collateral lethality ammunitions.

Usually, the killing range of fragment grenades can be effectively reduced and the harm to innocent people can be lowered by reducing the amount of charge, using non-metallic shells and other measures (Yang et al. 2018, Wang et al. 2020, Yu et al. 2023, Liang et al. 2017). However, these measures also lead to a smaller killing radius and a lower power of ammunition. Many studies have shown that the use of the sub-millimeter size of inert metal powder instead of fragments as the damage element in fragment grenades is an effective way to achieve low collateral damage. One method is to evenly mix the metal powder into explosives, forming heterogeneous explosives. When this kind of explosive explodes, the metal powder can produce a uniform metal powder flow with a high initial speed during detonation (Zhang et al. 2012, Frost et al. 2007). Many researchers have conducted in-depth studies on its gas-solid two-phase flow mechanism (Sugiyama et al. 2020, Xue et al. 2014, Zhang et al. 2001), sensitive conditions for particles through shock waves (Balakrishnan and Menon 2008), and detonation propagation and quenching rules (Ju and Law 2002). However, some studies have indicated that heterogeneous explosives containing metal particles are prone to producing hot spots when subjected to impacts, leading to the issue of munition safety. An alternative method, that is used in this research, is wrapping the metal particles around the explosives to form a dense powder ring that acts as a fragile shell. The warheads based on this structure are much safer because they can substantially reduce the possibility of producing local hot spots.

Many researchers have analyzed the killing effect of the metal particle cloud of this structure through experiments. Yao et al. (2010) compared the pressure curves after the explosions of a bare charge, non-metallic shell charge, and metal powder shell charge, and they found that the metal powder shell charge had a larger peak pressure and a significantly longer action time after an explosion, proving that the metal powder shell charge had a smaller killing area and a stronger killing effect within a smaller killing area. Chen et al. (2011) used the multi-layer paper target method to analyze the kinetic energy characteristics such as the number density, velocity and distribution of metal particle groups driven by the explosive. In previous experiments (Chen et al. 2017), it was found that metal particles were prone to sintering at the high temperature and pressure of detonation, resulting in uneven particle spatial distribution. Bai et al. (2010) evaluated the metal powder dispersion situation of different loading processes within an effective distance base on aspects such as the particle spatial number density, the particle penetration ability for the target plate, the process and safety. Furthermore, the addition of a dispersant is beneficial for reducing the possibility of metal powder sintering and agglomeration. Thus, the possibility of PTFE powder as an anti-sintering agent was explored based on this in this research.

The acceleration and dispersing process of metallic particles by the detonation of an explosive has been well studied. However, the penetration effects of high-speed metallic particles on human tissues have rarely been investigated. Gelatin is often used for a design that simulates human tissues (Liu et al. 2017, Moxnes et al. 2016, Liu et al. (2021b), Han et al. 2020) because its mechanical properties are close to those of human muscle. Thus, the ballistic impact into gelatin has become a conventional method for evaluating the ballistic wound of a human (Grimal et al. 2004). Gilson et al. (2020) conducted experiments analysis on the non-penetration ballistic response of a composite plate shielding gelatin block and evaluated the front surface deformation, pressure wave amplitude value, and duration of the gelatin block. Liu et al. (2021a) studied the translation and rotation of rifle bullets in ballistic gelatin. Wen et al. (2012) numerically studied the penetration of steel balls into gelatin. It was shown that the Lagrange solver had the highest calculation accuracy and efficiency. Ye et al. (2022) conducted dimensionless analysis and a finite element simulation on the penetration of medium-low speed millimeter-level steel balls into ballistic gelatin, which reproduced the experimental observation results well. Shuangshuang et al.(2020) developed an original numerical model based on SPH to study the dynamical phenomena during microscale impact of spheres into ballistic gelatin. Mitchell et al. (2003) described the results of an investigation into the impact of model micro-particles to ex vivo buccal mucosa (the cheek) of pigs and beagle dogs. Veysset et al. (2018) investigated the high-velocity impact response of gelatin and synthetic hydrogel samples using a laser-based microballistic platform for launching and imaging supersonic micro-particles. The above studies focused on the movement of millimeter-level projectiles in ballistic gelatin and the response of ballistic gelatin, but there have been relatively few studies on the damage effect of high number density micro-particles with smaller sizes on ballistic gelatin.

In this investigation, the penetration effects of the high number density metallic particles into ballistic gelatin were studied experimentally and numerically. Explosion experiments were first performed on a gelatin target using a tungsten particle ring filled with different-mass high-explosive charges. The numerical models of the tungsten particles penetrating the ballistic gelatin were established and validated by the experimental results of the penetration depths. Parametric studies were then carried out using this numerical model to determine the influence of the particle size and the spacing between two particles on the penetration depth and maximum cavity.

2 EXPERIMENTAL INVESTIGATION

2.1 Preparation of particle ring and charge

The materials for preparing dense particle rings include tungsten powder (average particle size: 300 μm, density: 19.35 g/cm^3) and PTFE powder (average particle size: 40 μm, density: 2.15 g/cm^3). Table 1 shows the physical properties of the two powders. The particle ring (ω_{PTFE}=13.3 %, ω_W=86.7 %) preparation process is shown in Figure 1. PTFE and tungsten powder are uniformly mixed for 15 minutes with a small drum mixer. Pour the mixed powder into a tool, and press with a pressure of 320 MPa for 3 minutes. The density of the particle ring was 7.99 g/cm^3.

Table 1 Properties of PTFE and tungsten powder.

Component	ρ (g/cm3)	Melting/Boiling Point (K)	Morphology	Size (μm)
PTFE	2.15	330/-	White powder	40 (±10)
Tungsten	19.35	3680/5828	Sliver-gray powder	300 (±100)

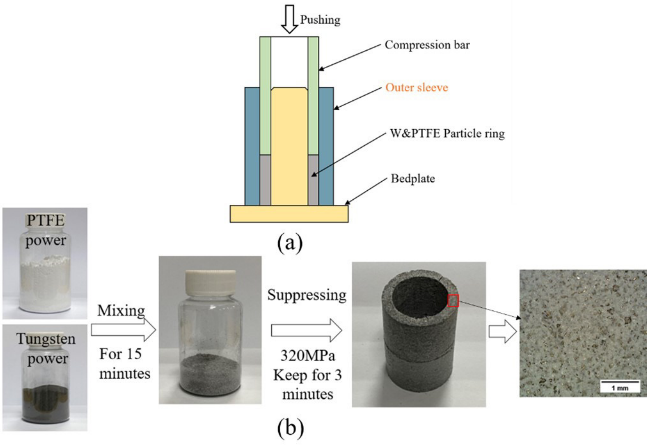

Figure 1 Particle ring preparation process: (a) mold for compressing the particle ring and (b) process of compressing the particle ring.

The particle ring was sheathed on the outer side of the JH-2 cylindrical explosive. The charge density was about 1.68 g/cm^3. Nylon was used for the top and bottom covers. Between the explosive and the particle ring, the outside of the particle ring is a CFRP shell for enhancing the overall strength. The specific structure is shown in Figure 2 (a). The charges were named D40, D80, and D93, as shown in Figure 2 (b). The number represents its outside diameter. The parameters of the particle ring and charge are shown in Table 2.

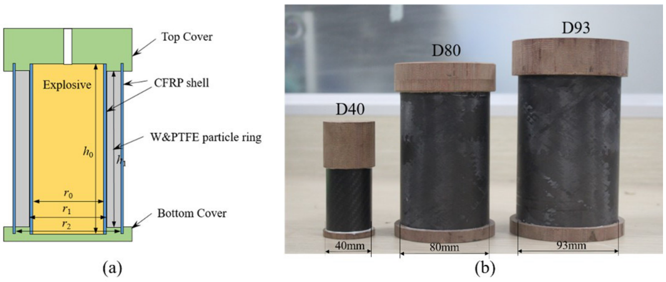

Figure 2 Three types of charged particle rings: (a) schematic diagram and (b) images.

Table 2 Sizes and mass of particle ring filled with charges.

	Explosive			Particle ring			
	Diameter	Height	Diameter	Height	Diameter	Height	Diameter
	r0(mm)	h0(mm)	r0(mm)	h0(mm)	r0(mm)	h0(mm)	r0(mm)
D40	25	60	49.8	27	37	55	220.9
D80	50	120	398.2	54	74	110	1767.1
D93	58	140	625.1	62.8	86	128.4	2772.9

2.2 Experimental set-up

The particle ring filled with charges was hung up vertically at the selected position, with the center 1.5 m from the ground. The three 10%wt gelatin blocks (side length was 300mm) were placed on three rigid support, as shown in Figure 3 (a) and Figure 3 (b). The supports were placed at a distance R_i from the blast center (where i =1, 2, 3). Each set of experimental detonation distances is determined by considering R_2, which is 40 times the maximum diameter of this structure. R_1 is less than 40 times the maximum diameter, while R_3 is greater than 40 times the maximum diameter, as indicated in Table 3. The field of the explosion experiment was arranged as shown in Figure 3 (c). The processes of explosive detonation and particle dispersion were recorded by a high-speed video recorder (6000 fps).

Table 3 The distances between the explosive centers of the three types of charges and their corresponding gelatin.

	D40	D80	D93
R_1(m)	1(<1600mm)	2(<3200mm)	3(<3720mm)
R_2(m)	1.6(=40mm×40)	3.2(=80mm×40)	3.72(=93mm×40)
R_3(m)	2.5(>1600mm)	4(>3200mm)	5(>3720mm)

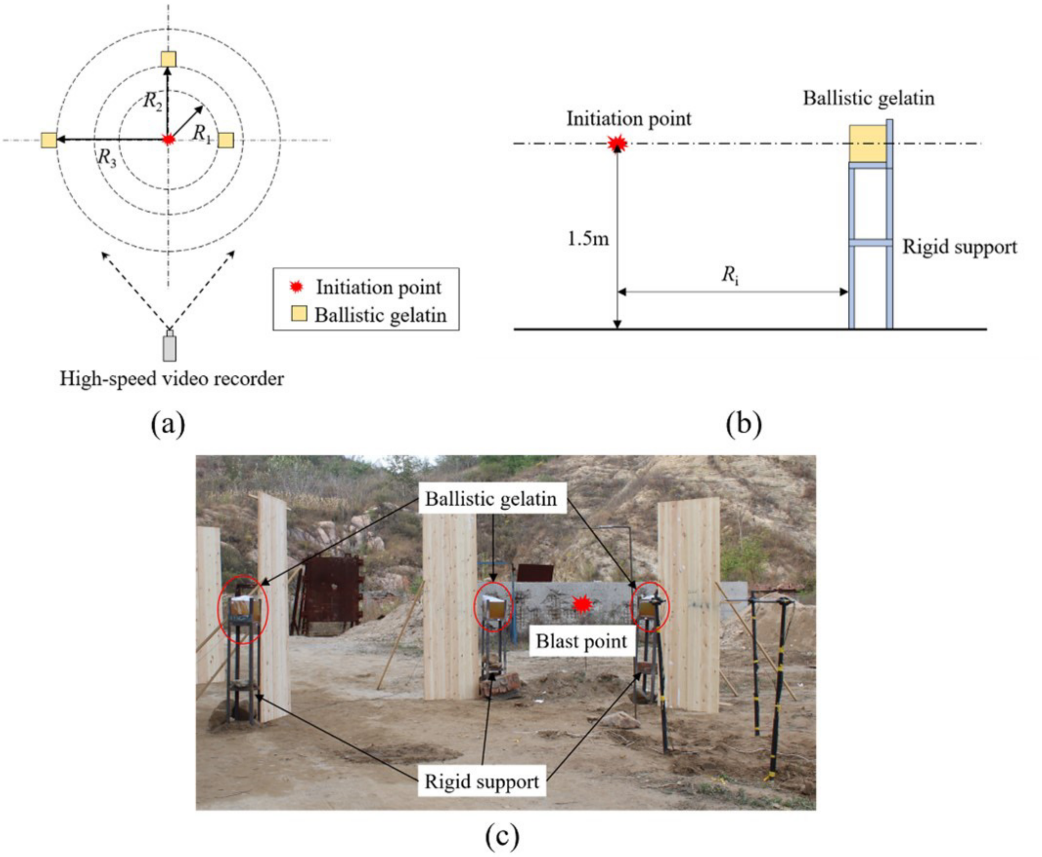

Figure 3 Explosion experiment set-up: (a) top view, (b) front view, and (c) actual explosion experiment field.

2.3 Experiment results and discussion

2.3.1 Particle cloud boundary initial velocity and decay

Figure 4 shows the typical explosion moments from the perspective of high-speed photography. The explosive volume expanded rapidly to form a high-temperature and high-pressure detonation product. The particle ring was compressed, and then expanded outward through momentum exchange with the detonation product. The particle ring broke into fragments, and then gradually detached from the detonation product. Due to the interface disturbance of the detonation products and the influence of the velocity gradient of the particle fragments, the particle fragments continued to break up and disperse to form particle flow. The arrival position of the powder boundary at various time intervals is delineated on the high-speed image, with reference to the baseline direction in Figure 4. The average radius from the explosion center to the cloud boundary was measured at different time points, as depicted in Figure 5.

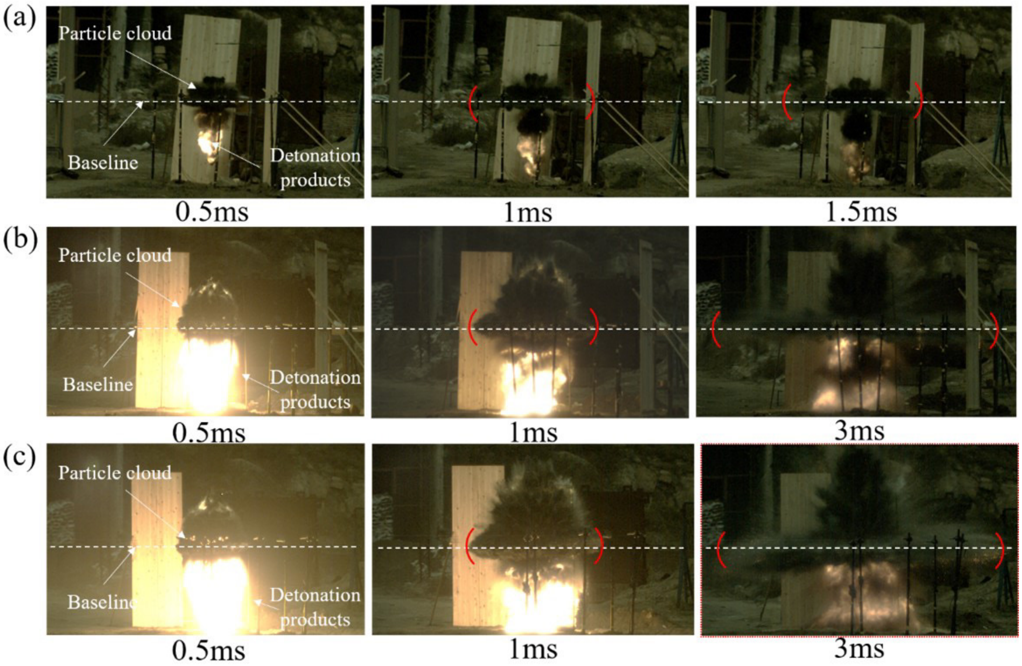

Figure 4 Explosion processes with three types of charges: (a) D40, (b) D80, and (c) D93.

The modified Gurney equation accounting for the initial velocity of particle cloud which is primarily a function of the mass ratio, the ratio between the particles and the charge.

$$v_0 = k\sqrt{2E}\sqrt{\frac{\lambda}{1+0.5\lambda}} \tag{1}$$

where $\lambda=m/m_p$, $\sqrt{2E}$ is a test constant that represents the performance of explosives, k is the energy loss coefficient considering the outflow of detonation gas. It was measured that the maximum throwing velocity of particles for the three cases were basically the same, at 1178.4 m/s, 1103.4 m/s, and 1138.3 m/s. The average speed of the three working conditions was 1140.0 m/s. It is finally determined that k is 0.89 which is more reasonable.

A simplified deceleration model was employed, assuming one-dimensional particle motion and disregarding inter-particle interactions. When the particles were imparted with a specific initial velocity to travel through still air, the primary influence on the particles was aerodynamic resistance. In accordance with aerodynamics, the equation governing particle motion could be derived as follows:

$$m_{p0}\frac{dv}{dt} = -\frac{1}{2}C_x\rho_{air}Av^2 \tag{2}$$

where m_{p0} is the mass of the particle, v is the velocity of the particle in the air, t is the time, C_x is the resistance coefficient, ρ_{air} is the air density, and A is the current windward area of the particle. The resistance coefficient C_x of a compressible viscous fluid flowing around a particle can be expressed as (Roache. 1976):

$$C_x = \frac{24\mu}{\rho_{air} d_p v} \tag{3}$$

where d_p is the particle size, and μ is the aerodynamic viscosity coefficient. At room temperature of 25 °C, μ is 0.01834 mPa·s. Then the relationship between the particle's velocity and time could be expressed as

$$v(t) = v_0 \exp(-\frac{t}{\tau_v}) \tag{4}$$

where $\tau_v = \frac{\varphi d_p^2 \rho_p}{18\mu}$ is the characteristic time of the velocity relaxation process and φ is the particle shape correction coefficient. As it approaches 1.00, the particle shape is closer to spherical. The initial velocity of the particle is v_0, and when t =0, $v(0)$ =v_0, and the particle cloud radius R_c could be expressed as

$$R_c(t) = v_0 \tau_v \left[1 - \exp(-\frac{t}{\tau_v})\right] \tag{5}$$

It is shown that when the initial velocity is constant, the change in the particle cloud radius with time depends on the particle size and density. The particles used in the experiments were identical. A series of results captured by high-speed photography were fitted to the particle shape correction coefficient φ by Eq. (5). The correction coefficient of the particle shape is φ=0.95, where R^2=0.995. It proves that the metal particles used in the experiment are relatively close to spherical. The curves of the particle cloud radius and particle velocity with time are shown in Figure 5.

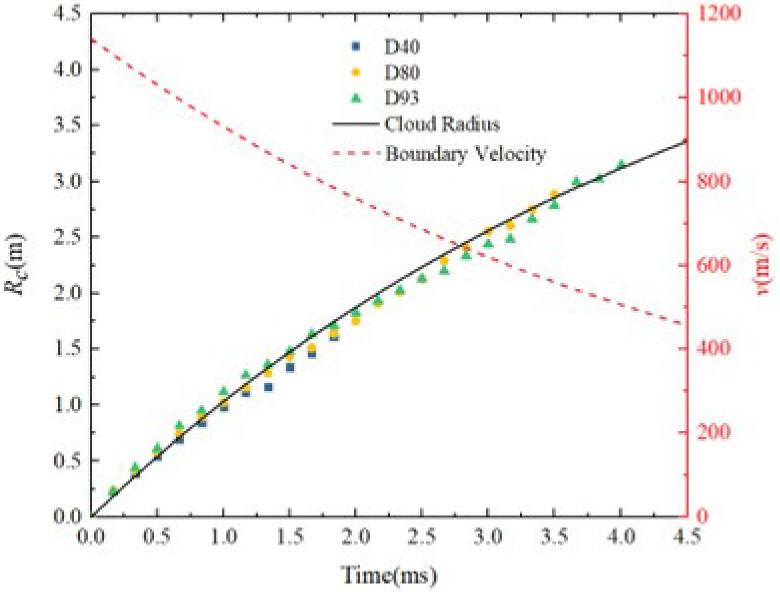

Figure 5 The change in particle cloud radius and boundary velocity over time, where the dispersed data points represent measurements from high-speed recordings. The black curve illustrates the variation of the particle cloud radius over time, while the red curve depicts the change in boundary velocity over time.

2.3.2 Penetration depth of particles into gelatin

The ballistic gelatin after the experiment was recovered, as shown in Figure 6. It could be clearly observed from the experiment results that a large number of small blind holes were present. These holes were evenly and densely distributed This phenomenon indirectly proved that the addition of PTFE powder to metal powder could effectively reduce the sintering and agglomeration of particles.

The embedding of the particles in the gelatin could be seen more clearly by shining bright light on the gelatin. Due to the influence of uncertain factors such as particle speed, particle size, shape and angle of incidence, the penetration depth of particles was different. The gelatin image was binarized, as shown in Figure 7. The black dots in the picture are particles stuck in the gelatin. The particle cloud boundary velocity and the corresponding gelatin penetration depth at different detonation distances are shown in Table 4.

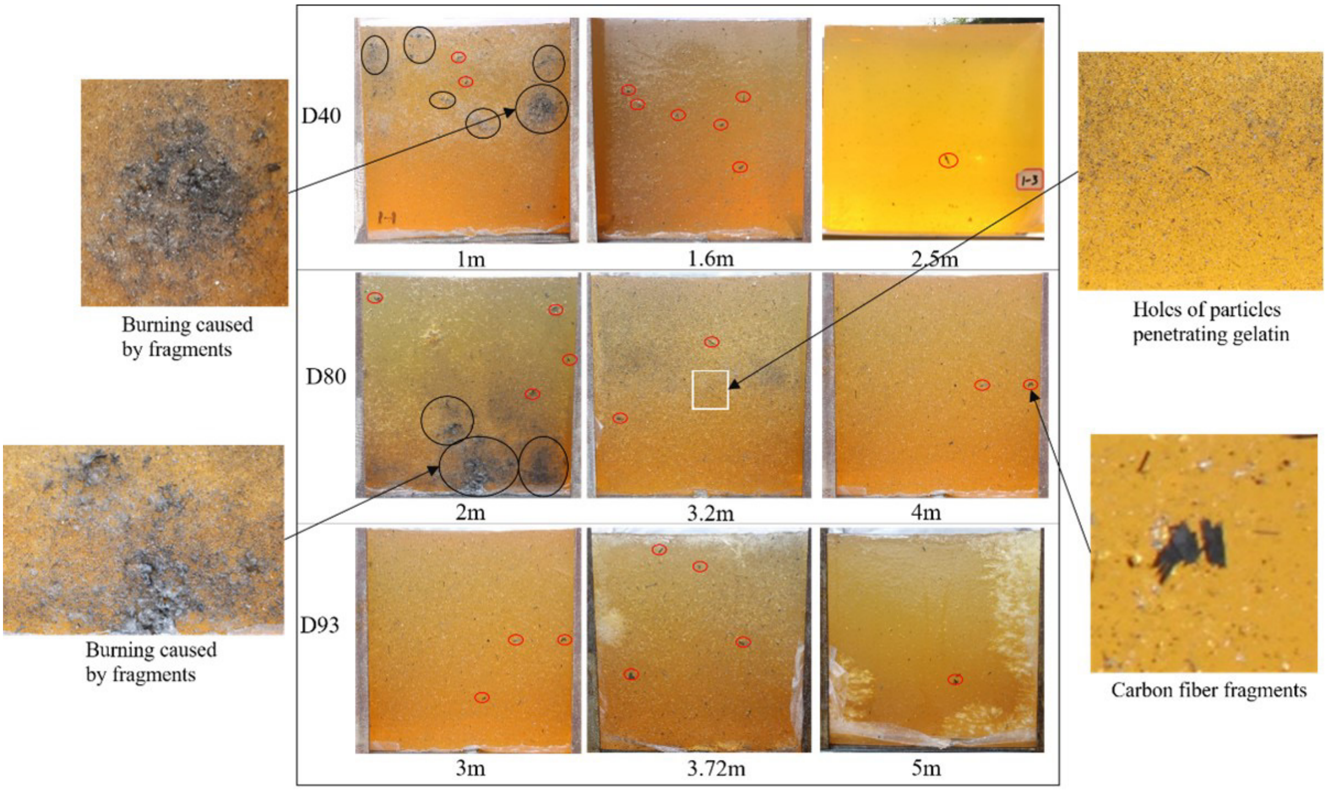

Figure 6 Results on the gelatin surface after the impact of the particle cloud. (Black circles represent burns caused by fragments, while red circles denote carbon fiber fragments. The concentrated black dots within the white box indicate the points where particles have penetrated the gelatin.)

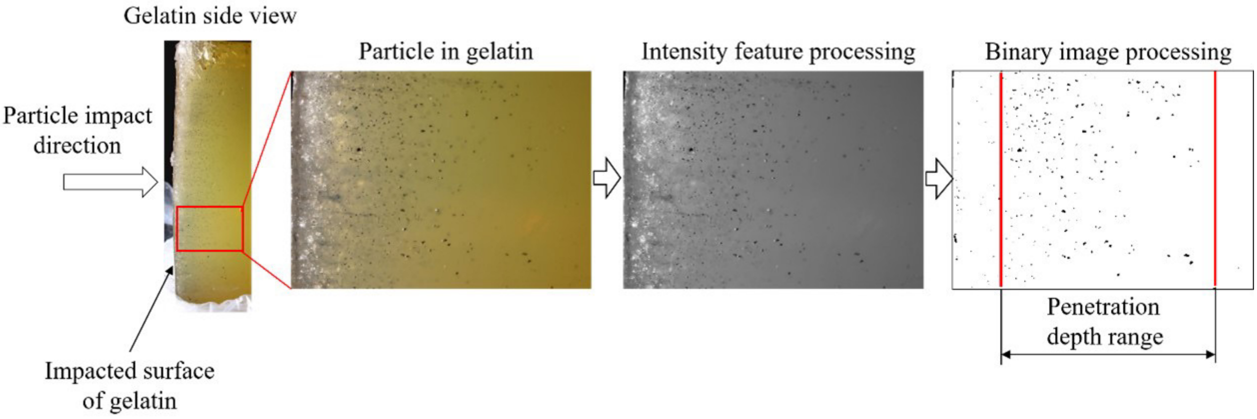

Figure 7 Binary image processing(The side of the gelatin target was processed. The results shown that the particle size range (300 ± 100 μm) results in a large range of penetration depths).

Table 4 Boundary velocity of the particle cloud at different detonation distances and the corresponding gelatin penetration depths.

No.	R_i (m)	Boundary velocity (m/s)	Minimum penetration depth (mm)	Maximum penetration depth (mm)
D40	1	907	10.6	55.7
	1.6	785	10.0	55.1
	2.5	601	9.3	48.6
D80	2	709	8.3	61.6
	3.2	460	8.4	56.6
	4	293	7.0	44.9
D93	3	500	9.3	55.6
	3.72	355	6.4	46.6
	5	103	5.3	22.9

2.3.3 Particle cloud spatial distribution

The particle cloud number density was obtained by recovering particles in gelatin. First, the gelatins after the experiments were placed in a water bath and heated to melt, and the liquid was allowed to stand for precipitation. The particles were precipitated as much as possible. After the removal of most of the clear solution in the upper layer, the remaining liquid was filtered with filter paper. The collected particles were washed repeatedly and dried to remove excess water. Finally, the mass of the tungsten particles in gelatin was obtained. The number density of particles is represented by the number of particles per unit area, and the results are shown in Figure 8. The factors affecting the number density of particles were mainly the mass of the particle ring and the detonation distance.

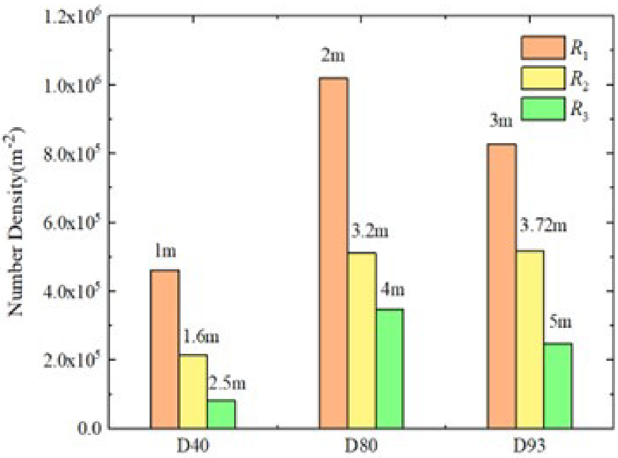

Figure 8 Number density by particle recovery at different distances (the average particle mass was approximately 1.13×10-4 g).

The geometric relationship of the particle cloud impacting the gelatin is shown in Figure 9. It was assumed that the distribution of the particle cloud in the circumferential direction was uniform. As shown in Figure 9 (a), the value of α is very small and can be approximated as a/R_i. a is the gelatin side length, m_W is the metal particle mass in the particle ring, and R_i is the detonation distance (i= 1, 2, 3). Then the particle mass in the projection m_α of angle α is

$$m_\alpha = \frac{a m_W}{2\pi R_i} \tag{6}$$

It is also assumed that the dispersion of the particle cloud in the axial direction is uniform and symmetrical along the horizontal plane of the center of the charge. As shown in Figure 9 (b), the area between two rays AA' and BB' is the dispersion range of the particle cloud. β is the angle between AA' and the horizontal direction, which represents the concentration of particle dispersion in the axial direction. The distance between A' and B' is L. β and L can be obtained from the geometric relationship that

$$\beta = \tan^{-1}(\frac{L - h_0}{2R_i}) \tag{7}$$

$$L = 2R_i \tan\beta + h_0 \tag{8}$$

Then the ratio of the particle mass m_G invading the gelatin to the particle mass m_α in the α angle is the ratio of the length of the *A’B’* segment to the size of the gelatin:

$$m_G = \frac{a}{L} m_\alpha \tag{9}$$

Substituting Eqs. (6), (7), and (8) into Eq. (9)

$$m_G = \frac{a^2 m_W}{4\pi R_i^2 \tan\beta + 2\pi R_i h_0} \tag{10}$$

The above equation shows the relationship between the particle mass m_G invading the gelatin and the total tungsten particle mass m_W and the distance R_i. When the particle recovery mass at different distances is known by the experiment, β can be obtained by Eq (9), as shown in Figure 10. The dispersion angle β is 13–14°. It could be concluded that the particle dispersion driven by the explosion of this structure is quite concentrated

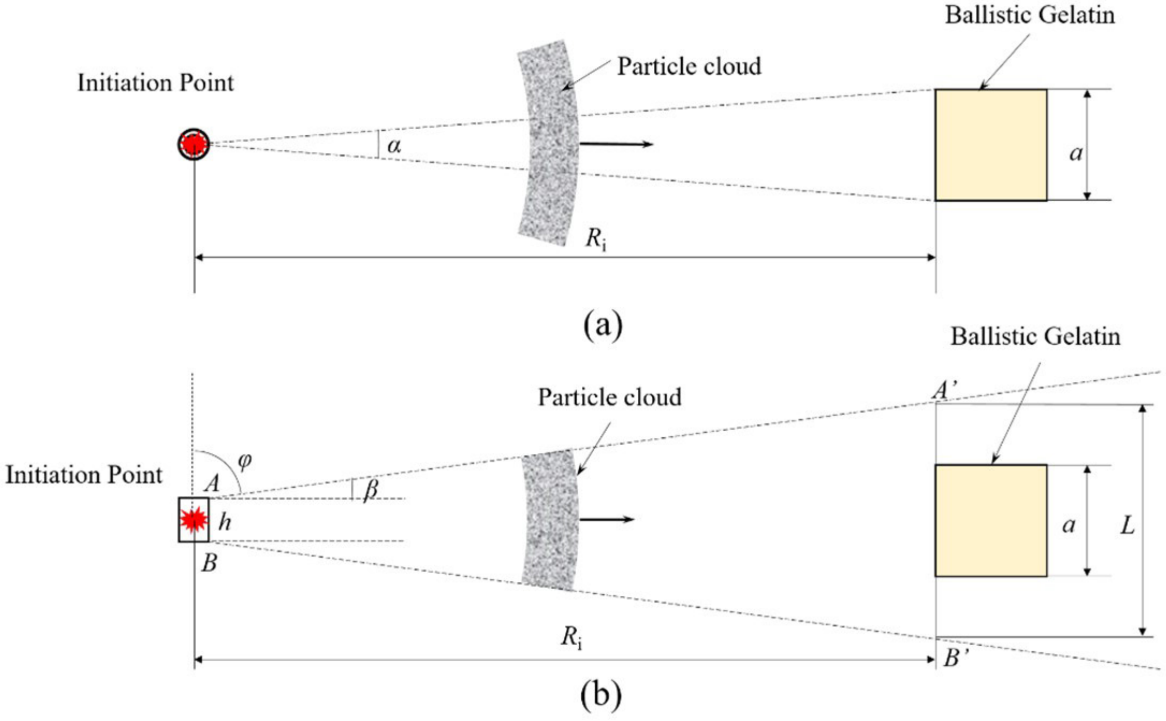

Figure 9 Geometric relationship of particle cloud dispersion: (a) Top view and (b) Front view

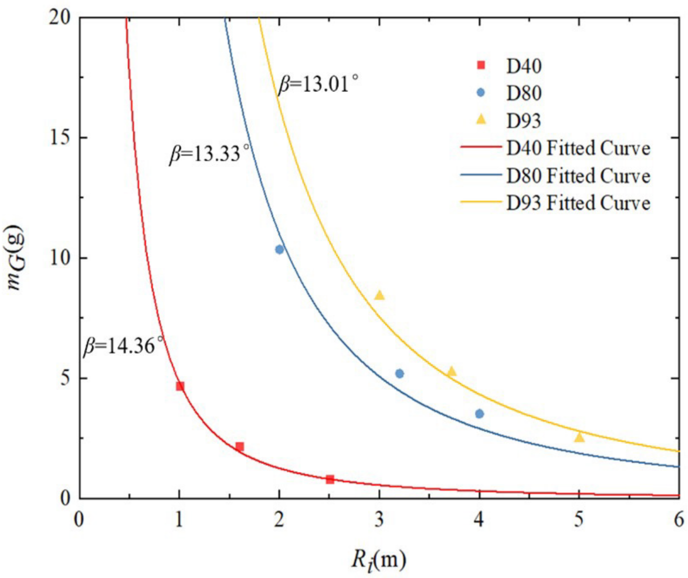

Figure 10 Particle extraction mass fitted by Eq. (10) (Fitting the experimental results to get β, D40 is 14.36°, D80 is 13.33°, D93 is 13.01°.)

3 NUMERICAL SIMULATION OF PARTICLE PENETRATION

3.1 Finite element model

The numerical simulation model of the particle penetration process was established using Ls-DYNA commercial finite element software. For submillimeter particles and gelatin blocks with large differences in size, it was unnecessary and a waste of computing resources to establish gelatin blocks of the same size as the experiment. It was only necessary to ensure that the gelatin established by the numerical simulation could reflect the temporary cavity expansion and elastic-plastic deformation region. In order to save computing resources, using a cylinder instead of a square model could effectively reduce the number of elements and increase the calculation speed. The geometric dimensions of the gelatin model were a cylinder of φ40mm, and the axial length was appropriately adjusted to ensure that the gelatin was not perforated. The Lagrange solver was used, and a three-dimensional 1/2 symmetric model was established.

One such discretization is exhibited in Figure 11 (a) and Figure 11 (b).: (I) The direct impact region within a diameter of 4 mm contained fine elements. (II) The elastic-plastic deformation region within a diameter of 12 mm contained medium elements. (III) The remaining region used coarse elements. Transition meshes were used between the three regional grids. This method could greatly reduce the number of meshes, ensure the regularity of the mesh shape, and improve computational accuracy. The tungsten particles were divided into six elements along the radial direction.

The CONTACT_ERODING_SURFACE_TO_SURFACE erosion contact definition was used to simulate the interaction between particles and gelatin. The viscous hourglass control algorithm with hourglass coefficient = 0.1 was employed. Symmetry constraints were set on the symmetry plane, and all the binding surfaces of gelatin and particles were considered non-traction except for mutual contact.

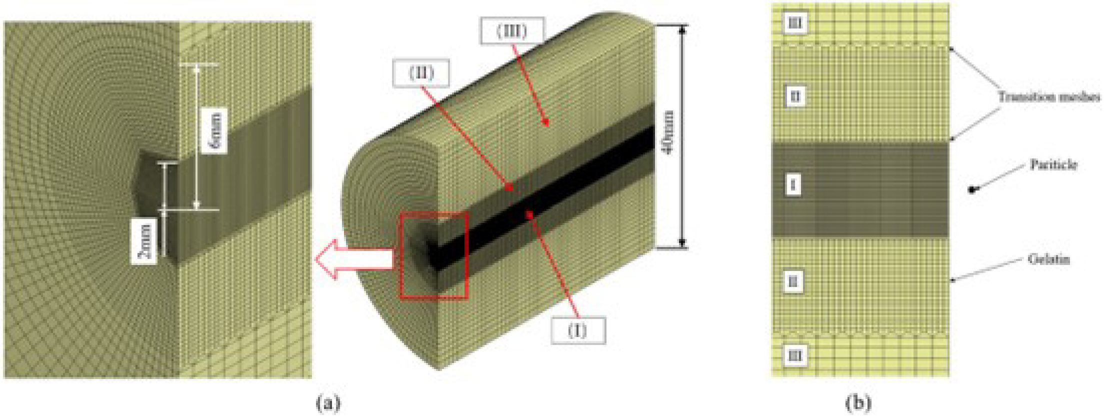

Figure 11 Gelatin and particle finite element model: (a) ballistic gelatin zone division and (b) discretization and transition meshes

3.2 Material model

The ballistic gelatin parameters of wt10% were measured by Wen et al. (2013). The density was 1.03 g/cm^3. The yield strength can be expressed as:

$$\sigma_y = \sigma_0 + \frac{E_t E}{E - E_t}\varepsilon_p \tag{11}$$

where σ_0 is the initial yield strength, ε_p is the effective plastic strain, E is Young's modulus, and E_t is the tangent modulus. The abovementioned constitutive relationship was supplemented as a polynomial of pressure P versus specific volume or density:

$$P = C_0 + C_1\mu + C_2\mu^2 + C_3\mu^3 \tag{12}$$

where μ is a dimensionless parameter that defines the ratio of the current density to the initial density, and C_0, C_1, C_2, and C_3 are constants.

Gelatin is described by the MAT_ELASTIC_PLASTIC_HYDRO strength model and the EOS_LINEAR_POLYNOMIAL equation of state. The specific material parameters are shown in Table 5.

Table 5 Material parameters of gelatin (Wen et al. 2013).

ρ (g/cm3)	***E* (kPa)**	***E_t* (kPa)**	***σ_0* (kPa)**	***C_0* (GPa)**	***C_1* (GPa)**	***C_2* (GPa)**	***C_3* (GPa)**
1.03	850	10	220	0	2.38	7.14	11.9

It was noted that the strength and stiffness of the tungsten material were much greater than that of gelatin. The particles were assumed to be rigid. The particle was described by MAT_RIGID. The material parameters are shown in Table 6.

Table 6 Material parameters of tungsten particles.

ρ (g/cm3)	**E (GPa)**	**μ**
19.35	344.7	0.303

3.3 Grid independence analysis

The elements within region (I) were directly affected by the particle impact, and the size of these elements played a crucial role in determining the penetration results. A grid-independent analysis of region (I) was conducted separately in both the radial and axial directions. The initial input conditions included a particle diameter of 0.3mm and an initial velocity of 700m/s.

Different numbers of meshes were employed in the radial direction: 20, 28, 36, 44, and 52, as illustrated in Figure 12 (a). Correspondingly, the radial element sizes were 0.100mm, 0.071 mm, 0.056 mm, 0.045 mm, and 0.038 mm. For the axial element size of 0.08mm, the time histories of numerically calculated penetration depths for these five finite element meshes are compared in Figure 13 (a). It is noteworthy that the difference between the calculated penetration depths decreases as the minimum element size in the gelatin finite element meshes diminishes. At t = 250 μs, the penetration depths of meshes with 36, 44, and 52 elements differ by less than 4%. Considering the trade-off between calculation speed and efficiency, the discretization with 36 elements (0.056mm) yields the optimal results.

In the axial direction, various grid sizes were used: 0.32 mm, 0.24 mm, 0.16 mm, 0.08 mm, and 0.04 mm, as depicted in Figure 12 (b). With a radial element size of 0.056mm, the time histories of numerically calculated penetration depths for these five finite element meshes are compared in Figure 13 (b). Remarkably, at t = 250 μs, the penetration depths of the 0.08 mm and 0.04 mm grids differ by less than 3%. In summary, the optimal grid discretization conditions entail a radial direction element size of 0.056mm and an axial direction element size of 0.08mm.

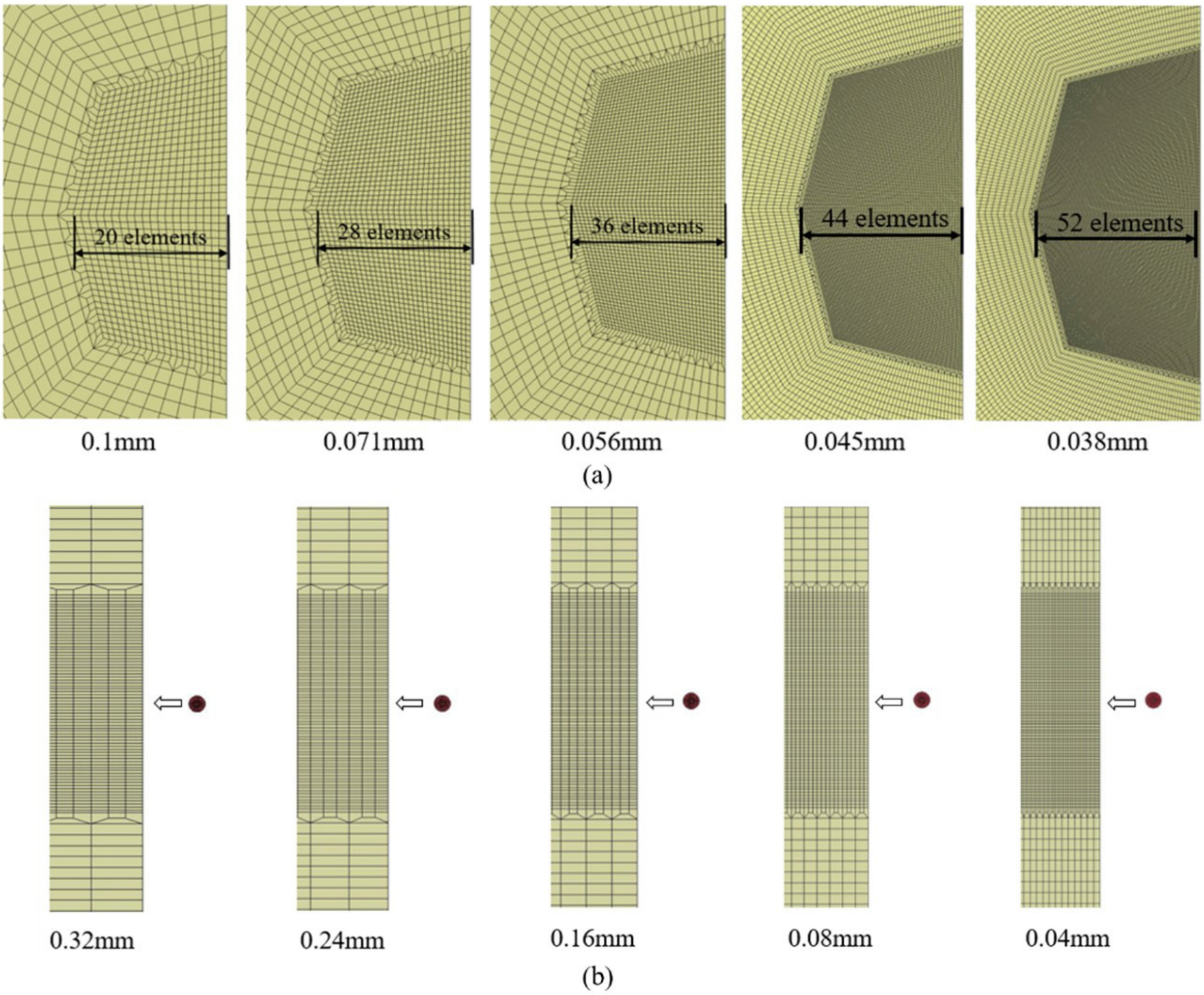

Figure 12 Grid partition of region (I):(a) Radial mesh independence analysis: In the axial direction, the element size is 0.08mm. In the radial direction, the same radius is divided into 20, 28, 36, 44, and 52 elements, corresponding to element side lengths of 0.1mm, 0.071mm, 0.056mm, 0.045mm, and 0.038mm.(b) Axial mesh independence analysis: In the radial direction, the element size is 0.056mm. In the axial direction, the element side lengths are 0.32mm, 0.24mm, 0.16mm, 0.08mm, and 0.04mm.

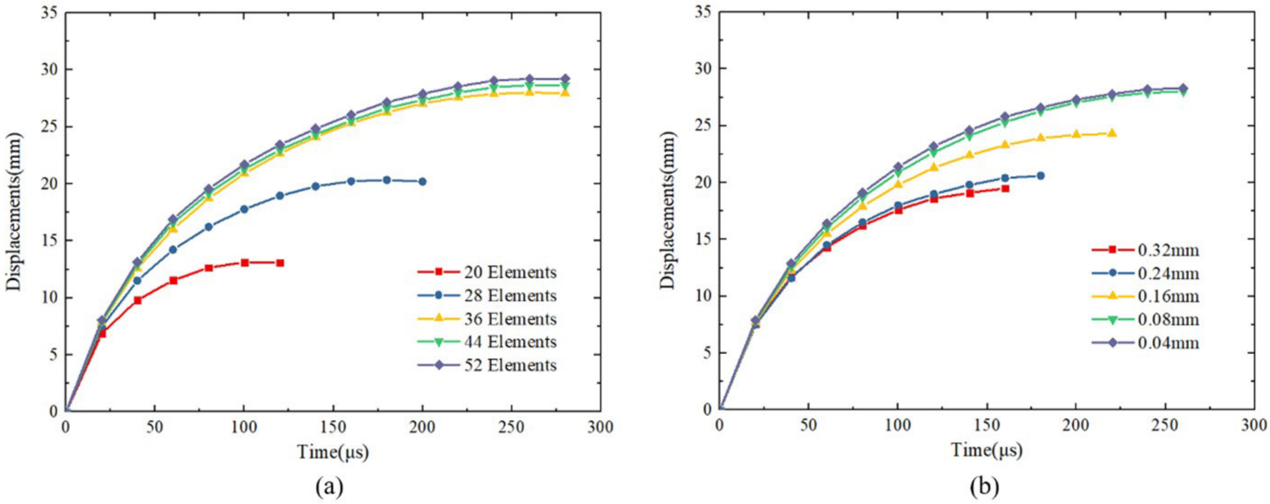

Figure 13 Grid independence result: (a) In the radial direction, the discretization with 36 elements (0.056mm) yields the optimal results. (b) In the axial direction, the discretization with 0.08mm yields the optimal results.

3.4 Results and discussion

3.4.1 Particle movement and cavity expansion

Simulation experiments were conducted to assess the accuracy of the numerical simulations in modeling single particle penetration. These simulations considered a range of particle velocities and sizes. Specifically, particle penetration scenarios were simulated for particles with diameters spanning from 0.2mm to 0.4mm, corresponding to characteristic velocities within the range of 103 m/s to 907 m/s (as indicated in Table 4). Figure 14 illustrates typical images of particle penetration, with particle sizes of 0.3mm and velocities of 500m/s, showcasing the formation of a temporary cavity characterized by the maximum diameter ($d_{\max}$) and the maximum penetration depth ($x_{\max}$).

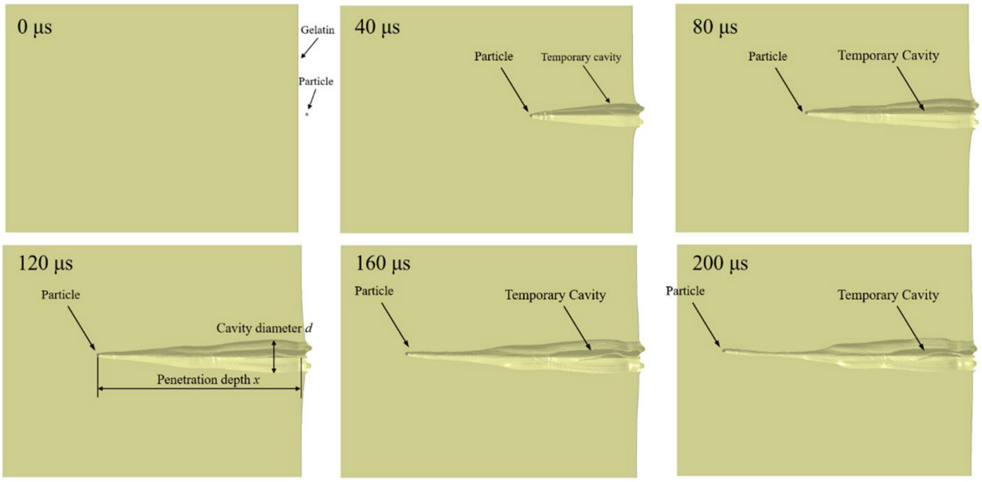

Figure 14 Typical moments of particle penetration into gelatin (particle size is 0.3mm and velocitiy is 500m/s)

The viscous fluid resistance model (Swain et al. 2014) of projectiles penetrating gelatin proposed is used to describe the maximum penetration depth of particles. It is suitable for the problem of a projectile penetrating gelatin in 100-1500 m/s, with consideration of the inertia resistance and viscous resistance of gelatin. The force of sub-millimeter particles in gelatin can be described as

$$-m_{p0}\frac{dv}{dt} = \rho S C_1 v^2 + \frac{\mu}{b} S C_V v \tag{13}$$

where m_{p0} is the particle mass, v is the particle velocity, ρ is the gelatin density, S is the cross-sectional area, C_1 is the inertial resistance coefficient, and C_v is the viscous resistance coefficient. μ is the velocity coefficient, b is the boundary layer thickness, and μ and b are unknown parameters related to the gelatin material. $A=-\rho C_1 S/m_{p0}$, $B=-\mu C_v S/bm_{p0}$. The relationship between the maximum penetration depth $x_{\max}$ and the initial velocity v_0 of particles penetrating gelatin is obtained as

$$x_{\max} = \frac{1}{A}\ln\left(\frac{B}{Av_0 + B}\right) \tag{14}$$

The maximum temporary cavity can be considered directly proportional to the particle diameter (d_p) and initial velocity (v_0):

$$d_{\max} = K d_p v_0 \tag{15}$$

where K is a cavity expansion coefficient.

Figure 15 (a) uses the viscous fluid resistance model to fit the numerical simulation results of the maximum penetration depth of particles with three different particle sizes from 0.2mm to 0.4mm into gelatin. The fitting values of A are -73.050, -48.479, and -36.525 respectively. The fitting values of B are -28863.380, -9322.929, and -4232.273 respectively.

The particle mass m_{p0} and cross-sectional area S are known. C_1 is the inertial resistance coefficient, and the C_1 values of the three particle sizes are 0.183, 0.182, and 0.183 respectively. The inertial drag coefficient has nothing to do with particle size. The value of $\mu C_v/b$ is related to gelatin viscosity and boundary layer thickness, and $\mu C_v/b$ decreases with the increase of particle size.

Since it was not possible to directly observe the size of the temporary cavity in the gelatin during the *simulation*s, Figure 15 (b) provides an analysis of the numerical simulation results for the temporary cavity diameter. According to the simulation results, the curve between the initial velocity v_0 and the maximum temporary cavity diameter d_{max} is obtained by least squares fitting, as shown in Figure 15(b). Among them, the fitted K values are 26.35, 27.8 and 31.9 respectively.

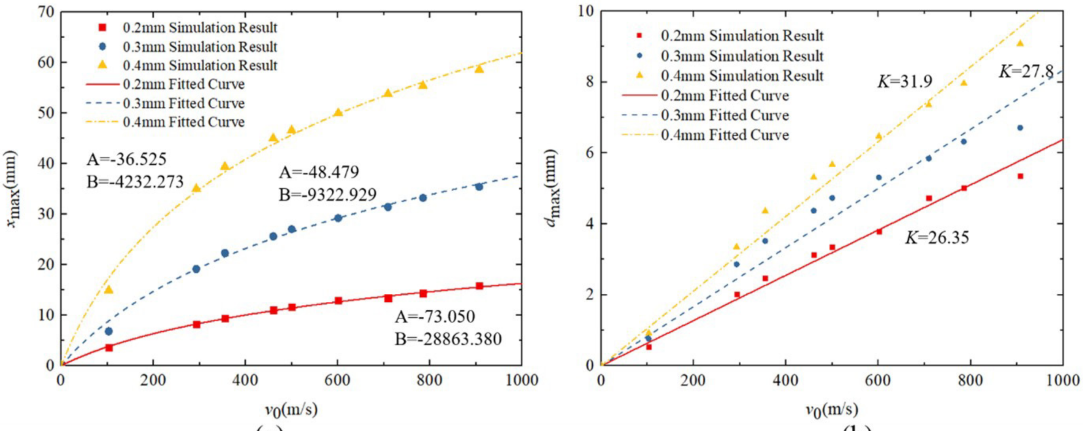

(a) (b)

Figure 15 The fitting curve of the simulation results: (a) Maximum penetration depth and (b) Maximum temporary cavity diameter

3.4.2 Numerical simulation verification

In Figure 16, a comparison is made between experimental results and numerical simulation results for the maximum penetration depth (x_{max}) under the same velocity and particle diameter conditions. The experimental results represent the depths at which particles with diameters of 0.2 and 0.4 mm penetrate into the gelatin at speeds ranging from 103 m/s to 907 m/s. Upon comparing the numerical simulation with the experimental results, significant differences are observed at low velocities, but the experimental and numerical results converge at higher speeds. It is also noticeable that there are substantial differences between the experimental and numerical results for larger particle diameters, while they are relatively close for smaller diameters. When comparing the depth range of particle distribution between experimental and numerical simulation results, the average error is 30%. Possible sources of errors mainly include: human errors caused by inconspicuous image differences between small-sized carbon fiber fragments and particles, random errors in the binary identification process, and accidental errors in particle penetration during the intrusion process. The former resulted in errors in the measurement of the penetration depth of particles, while the latter led to an increase in the penetration depth of particles at higher velocities.

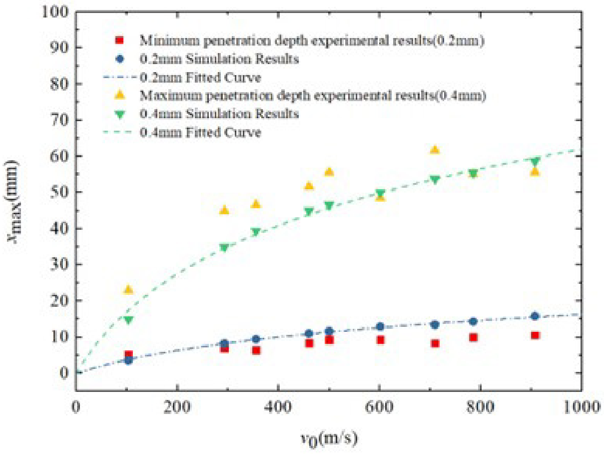

Figure 16 Comparison of numerical simulation and experimental penetration results

4 DOUBLE-PARTICLE PENETRATION AND CAVITY INTERFERENCE

The presence of temporary cavities formed by the particle cloud during gelatin penetration could introduce interference. In order to explore the potential coupling effect during the penetration of dense particles into gelatin, simulations were conducted involving two particles with equal diameters and velocities of 300 m/s, 500 m/s, 700 m/s, and 900 m/s. Figure 17 shows typical moments of double-particle penetration into gelatin, with particle sizes of 0.3mm and velocities of 500m/s. In the simulations, it was observed that the gelatin in the central region of the cavity was subjected to fractures and breakages, which were attributed to the tension and collision of stress waves. These effects were manifested as element failures and deletions within the numerical simulation.

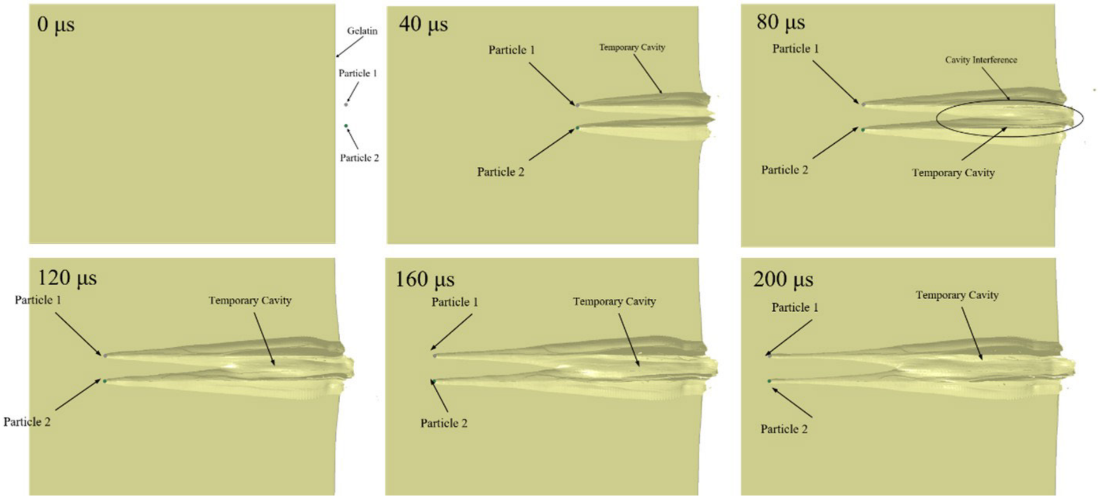

Figure 17 Typical moments of double-particle penetration into gelatin (particle sizes are 0.3mm and velocities are 500m/s)

It could be known that when the initial spacing between the two particles was large, the interference behavior would not occur. Then there had to be a case in which the cavity generated by the two particles did not interfere. This space could be named the critical cavity interference distance Δy. Ideally, the critical cavity interference distance should be exactly the size of the largest temporary cavity diameter of a single particle, that is $\Delta y = d_{\max}$. Due to the transmission of a stress wave in gelatin, the expansion environment of adjacent cavities changes, which may make the critical cavity interference distance different from the maximum temporary cavity diameter. Therefore, numerical simulations were carried out for different particle spacing situations.

By comparing the penetration results of a single particle and double particles, it was found that the penetration depth of the double particle was basically consistent with that of the single particle and had nothing to do with the particle spacing, as shown in Figure 18. Submillimeter particle cloud has no coupling effect on the penetration depth of gelatin.

It could be seen that as the distance between particles increased, the process of a temporary cavity from interference to non-interference is shown in Figure 19. The numerical simulation results showed that the critical cavity interference distance was smaller than the maximum temporary cavity diameter, $\Delta y < d_{\max}$, as shown in Table 7.

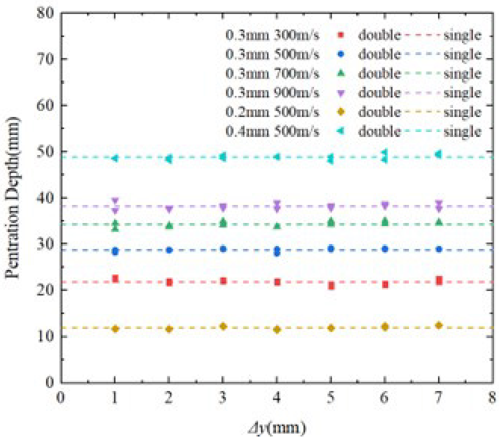

Figure 18 Comparison of double-particle penetration depth and single-particle penetration depth

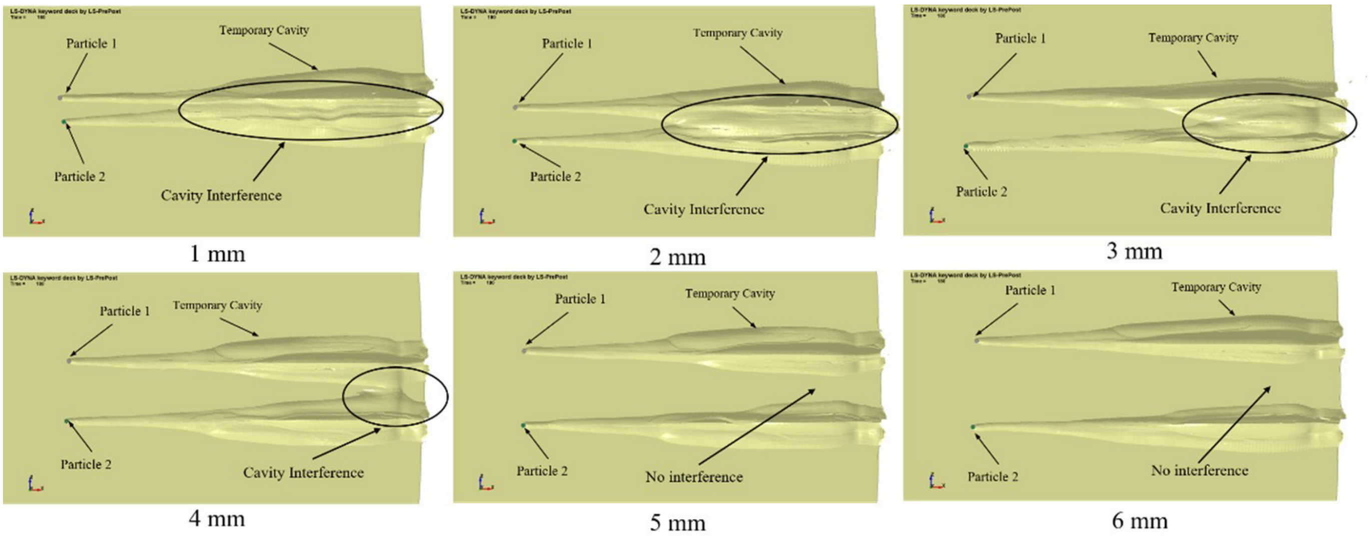

Figure 19 Effect of particle spacing on cavity interference (particle sizes are 0.3mm and velocities are 700m/s)

Table 7 Maximum temporary cavity diameter and critical cavity interference distance

Initial velocity v_0 (m/s)	Particle diameter (mm)	Maximum temporary cavity diameter d_{max}(mm)	Critical cavity interference distance Δy(mm)
300	0.3	2.86	2–2.5
500	0.3	4.73	4–4.5
700	0.3	5.84	5–5.5
900	0.3	6.71	6–6.5
500	0.2	3.35	3–3.5
500	0.4	5.67	5–5.5

A possible explanation for the phenomenon described above can be offered. During particle penetration, an extremely high pressure is generated in the region surrounding the particle contact surface. This pressure propagates both radially and axially, as illustrated in Figure 20 (a). The shock pressure wave on one side exerts a force that deforms the gelatin within the cavity on the opposite side, subsequently causing the gelatin adjacent to the cavity to be displaced into the cavity. This expansion and compression between the two particles result in a narrowing of the cavity, leading to the observed effect, as depicted in Figure 20 (b). As indicated in the illustration, the temporary cavity exhibits asymmetry, which results in a critical cavity interference distance smaller than the maximum diameter of the temporary cavity during single-particle penetration.

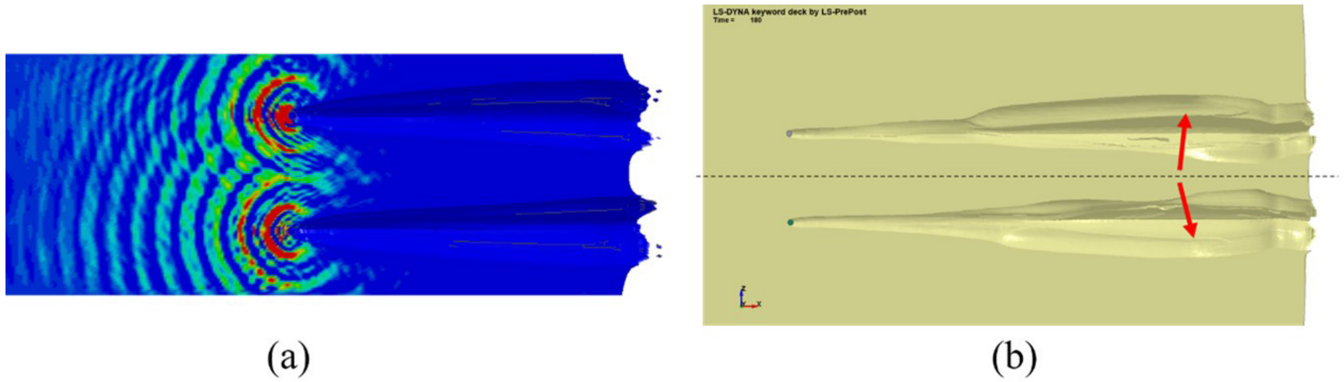

Figure 20 Gelatin in double-particle penetration: (a) Pressure propagation in contact surface and (b) Temporary cavity compression

5 CONCLUSIONS

The following main conclusions are obtained:

(1) The experimental results obtained from high-speed video recordings of ballistic gelatin reveal the uniformity of the particle cloud generated by the PTFE and tungsten powder particle ring driven by detonation. It was observed that metal particles did not undergo sintering or agglomeration under high-temperature and high-pressure detonation conditions. This demonstrates the potential use of PTFE as an anti-sintering agent in metal powder ammunition.

(2) This study has explored the penetration characteristics of ballistic gelatin by a dense particle cloud propelled by detonation. The particle number density distribution in space was determined by analyzing the particle mass embedded in the gelatin. Utilizing the assumption of uniformity and geometric relationships, the range of particle cloud dispersing angles was calculated, showing good agreement with experimental results.

(3) The research involved numerical simulations to determine the maximum penetration depth and temporary cavity diameter for different characteristic velocities and particle sizes. The deviation of numerical simulation results from experimental data fell within an acceptable range. A model considering gelatin viscous penetration was employed to describe particle penetration, with calculated results matching the simulation outcomes. Further numerical simulations were conducted to address the cavity interference problem between two particles of the same size and velocity, based on single-particle penetration. The results indicated that the critical cavity interference distance (Δy) was typically smaller than the maximum temporary cavity diameter ($d_{\max}$) of a single particle.

6 ACKNOWLEDGMENTS

The authors acknowledge the financial support of the National Natural Science Foundation of China (12102198).

Author's Contributions: Writing - original draft, Weihang Li; Writing - review & editing, Weihang Li and Wei Zhu; Conceptualization, Wenjin Yao; Funding acquisition, Wei Zhu; Supervision, Dacheng Gao, Shilei Tian, Chao Han and Yangyang Liu.

Editor: Marcílio Alves

References

Bai, C. H., Chen, Y. H., Li, J. P., Wang, Z. Q., Liu, L. (2010). Charge forms for explosion dispersal of metal particles. Explosion and Shock Waves, 30(6):652-657.

Balakrishnan, K., Menon, S. (2008). Simulation of Blast Wave Propagation and Particle Motion from Detonation Containing Dense Inert Particles. In 44th AIAA/ASME/SAE/ASEE Joint Propulsion Conference & Exhibit (p. 4689).

Chen, X., Li, X., Yan, H., Wang, X., & Miao, Y. (2017). Explosive compact-coating of tungsten–copper alloy to a copper surface. Materials Research Express, 4(3), 036502.

Chen, Y. H., Bai, C. H., Liu, Y., Wang, Z. Q., Li, J. P. (2011). Assessment on Kinetic Characteristics of Granular Swarm Dispersed by Explosion. Chinese Journal of Explosives & Propellants, 34(4), 45-48.

David Veysset, Steven E. Kooi, A.A. Maznev, Shengchang Tang, Aleksandar S. Mijailovic, Yun Jung Yang, Kyle Geiser, Krystyn J. Van Vliet, Bradley D. Olsen, Keith. A. Nelson. (2018). High-velocity micro-particle impact on gelatin and synthetic hydrogel. Journal of the Mechanical Behavior of Biomedical Materials, 86,71-76.

Frost, D. L., Ornthanalai, C., Zarei, Z., Tanguay, V., Zhang, F. (2007). Particle momentum effects from the detonation of heterogeneous explosives. Journal of Applied Physics, 101(11):115-937.

Gilson, L., Rabet, L., Imad, A., & Coghe, F. (2020). Experimental and numerical assessment of non-penetrating impacts on a composite protection and ballistic gelatin. International Journal of Impact Engineering, 136, 103417.

Grimal, Q., Gama, B. A., Naili, S., Watzky, A., & Gillespie Jr, J. W. (2004). Finite element study of high-speed blunt impact on thorax: linear elastic considerations. International Journal of Impact Engineering, 30(6), 665-683.

Han, R. G., Qu, Y. J., Yan, W. M., Qin, B., Wang, S., & Wang, J. Z. (2020). Experimental study of transient pressure wave in the behind armor blunt trauma induced by different rifle bullets. Defence Technology, 16(4), 900-909.

Ju, Y., Law, C. K. (2002) Law. Propagation and quenching of detonation waves in particle laden mixtures. Combustion and flame, 129(4), 356-364.

Liang, B., Zhou, J. Q., Feng, G. P., Lu, Y. G. (2017). Experimental research on blast power of fiber reinforced anti-hard target warhead. Defence Technology, 13(3), 212-218.

Liu, K., Ning, J., Wu, Z., Ren, H., Jiang, M. (2017). A comparative investigation on motion model of rifle bullet penetration into gelatin. International Journal of Impact Engineering, 103:169-179.

Liu, L., Ding, C., Wang, P., Zhang, X., & Lu, Q. (2021a). Yawing motion of rifle bullets penetrating into ballistic gelatin. International Journal of Impact Engineering, 156, 103960.

Liu, L., Fan, Y., Wang, P., Zhang, X., & Lu, Q. (2021b). A resistance force model for spherical projectiles penetrating ballistic gelatin based on cavity expansion theory [J]. Proceedings of the Institution of Mechanical Engineers, Part C. Journal of mechanical engineering science, 235(17), 3135-3145.

Moxnes, J. F., Frøyland, Ø., Skriudalen, S., Prytz, A. K., Teland, J. A., Friis, E., & Ødegårdstuen, G. (2016). On the study of ricochet and penetration in sand, water and gelatin by spheres, 7.62 mm APM2, and 25 mm projectiles [J]. Defence Technology, 12(2), 159-170.

Roache, P.J. (1976) Computational fluid dynamics. Mathematics of Computation.

Shuangshuang, M., Taddei, L., Lebaal, N., Veysset, D., Roth, S. (2020). Modeling micro-particles impacts into ballistic gelatin using smoothed particles hydrodynamics method. Extreme Mechanics Letters, 39, 100852.

Sugiyama, Y., Homae, T., Matsumura, T., Wakabayashi, K. (2020). Numerical study on the attenuation effect on the blast wave of encircling a high explosive with granular mediax. Journal of Applied Physics, 127(16).

Swain, M. V., Kieser, D. C., Shah, S., Kieser, J. (2014) A. Projectile penetration into ballistic gelatin. Journal of the Mechanical Behavior of Biomedical Materials Volume 29, 385-392.

Thomas J Mitchell, Mark AF Kendall, Brian J Bellhouse. (2003). A ballistic study of micro-particle penetration to the oral mucosa. International Journal of Impact Engineering, 28(3), 581-599.

Walsh, J I. (2014). Precision Weapons, Civilian Casualties, and Support for the Use of Force. Political Psychology, 36(5), 507-523.

Wang, W. Z., Chen, Z. G., Feng, S. S., Zhao, T. Y. (2020). Experimental study on ceramic balls impact composite armor. Defence Technology, 16(2), 408-416.

Wen Y K, Xu C, Chen A J, Shi X N. (2012). Numerical simulation of spherical fragments penetrating into ballistic gelatin at high velocity. Journal of Ballistics, 24(3), 25-30.

Wen, Y., Xu, C., Wang, H., Chen, A., Batra, R. C. (2013) Impact of steel spheres on ballistic gelatin at moderate velocities. International Journal of Impact Engineering, 62, 142-151.

Xue, K., Yu, Q., Bai, C. (2014). Dual fragmentation modes of the explosively dispersed granular materials. The European Physical Journal E, 37, 1-12.

Yao, W. J., Wang, X. M., Li, W. B. (2010). Effect of Metal Powder on Blast Power of the Low Collateral Damage Ammunition. Advanced Materials Research, 97, 547-551.

Yang, S. Q., Sun, C. J., Qian, L. X., Wei, J. (2018). Experimentation and Fragment Flight Analysis of Low-Collateral-Damage Warhead with Nonmetal Shell. Chinese Journal of High Pressure Physics, 32, 134-138.

Ye, S. J., Xu, Y. F., Zhou, Y., Cheng, J. C., Huang, J. Y., Cai, Y., Luo, S. N. (2022). Penetration dynamics of steel spheres into a ballistic gelatin: Experiments, nondimensional analysis, and finite element modeling. International journal of impact engineering, 162, 104144.

Yu, W. H., Li, W. P., Shangguan, Y. F., Ji, X. Y., Ma, T., Wu, G. Q. (2023). Relationships between distribution characteristics of ceramic fragments and anti-penetration performance of ceramic composite bulletproof insert plates. Defence Technology.

Zhang, F. (2012). Metalized heterogeneous detonation and dense reactive particle flow. AIP Conf. Proc. 29 March 2012; 1426 (1): 27–34.

Zhang, F., Frost, D. L., Thibault, P. A., Murray, S. B. (2001). Explosive dispersal of solid particles. Shock Waves, 10(6), 431-443.